Crustal anisotropy beneath Hudson Bay from ambient-noise interferometry

Agnieszka Pawlak and David W. Eaton

ABSTRACT

Hudson Bay overlays complicated tectonic structures for which new insights have only recently been emerging. Using azimuthal anisotropy (or HTI) results in conjunction with isotropic group velocity maps, we focus our study on the formation and regional crustal structure beneath Hudson Bay. Twenty-one months of continuous ambient-noise recordings have been acquired from 37 broadband seismograph stations that encircle Hudson Bay. These stations are part of the Hudson Bay Lithospheric Experiment (HuBLE), an international project that is currently operating more than 40 broadband seismograph stations around the periphery of Hudson Bay. The inter-station group-velocity dispersion curves found from ambient-noise interferometry, are input into tomographic inversion for azimuthally anisotropic group-velocity maps, which reveal structural fabric in the crust.

This work marks the first study where solely ambient seismic noise data have been considered in azimuthal anisotropy work. As such, extensive parameter and resolution testing is done to assess model feasibility. Results show mid-crustal anisotropy patterns correlating well with regional geology, with a profound change along the suture between the Churchill and Superior plates that collided ca. 1.8 Ga during the final stages of assembly of Laurentia: the Trans Hudson Orogen. The lower crust/upper mantle results, however, show a significant transition in anisotropic fast direction and a more complicated anisotropic fabric, also with a profound change along the suture zone. The data are also compared with regional crustal magnetics and show a significant similarity at periods sampling the mid-crust, but not the lower crust.

INTRODUCTION

Hudson Bay is a shallow inland sea that overlies the Paleozoic Hudson Bay basin, an intracratonic basin with stratigraphic record similar to the hydrocarbon-rich Williston, Illinois and Michigan basins. The Precambrian basement underlying the Hudson Bay basin was assembled by continental collisions culminating with the ca. 1.8 Ga Trans-Hudson Orogen (THO; Eaton and Darbyshire 2010). Whether or not the THO and earlier collisional events are preserved as fossil fabrics beneath the Bay remains unclear. Loading by the Laurentide ice-sheet, and subsequent on-going glacial rebound may also manifest as measurable seismic anisotropic fabrics beneath the Bay. To address these issues, we investigate crustal anisotropy and seismic-velocity structure using ambient-noise tomography (or seismic interferometry), using 21 months of continuous data acquired at 37 broadband seismograph stations located around the periphery of Hudson Bay (FIG 1a). This study builds on earlier work (Pawlak et al. 2011) in which the isotropic seismic structure of the crust and upper mantle beneath Hudson Bay was

imaged using the method of Bensen et al. (2007). Although ambient-noise tomography has been widely used in recent years (e.g., Shapiro et al. 2005; Curtis et al., 2006; Yao et al., 2006; Yang et al. 2007; Moschetti et al. 2007; Lin et al. 2007, 2010), our study is one of the first to incorporate seismic anisotropy into the analysis.

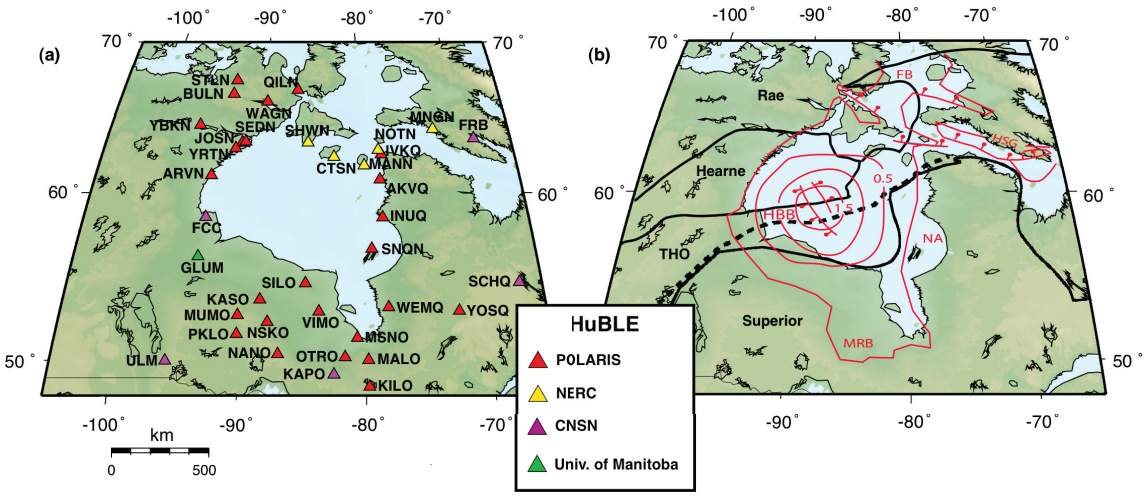

FIG 1. (a) Map of Hudson Bay showing all HuBLE stations used in this study. (b) Tectonic map of Hudson Bay. Solid black lines are approximate locations of tectonic boundaries and the dashed black line represents the suture zone. Abbreviations are as follows: THO, Trans-Hudson orogen; FB, Foxe basin; HSG, Hudson Strait graben; HBB, Hudson Bay basin; NA, Nastapoka Arc; MRB, Moose River basin (after Eaton and Darbyshire 2010).

Our investigation uses continuous recordings of ground motion from broadband seismograph stations deployed as part of the Hudson Bay Lithospheric Experiment (HuBLE), an international initiative with the broad aim of elucidating the lithospheric architecture beneath the Bay. To date, HuBLE data have been used to study various features and depth ranges, including receiver-function analysis of crustal structure (Thompson et al 2010) and mantle transition zone thickness (Thompson et al 2011), isotropic ambient-noise tomography to investigate basin structure (Pawlak et al., 2011), SKS-splitting investigation of upper-mantle anisotropy (Bastow et al. 2011) and surface-wave studies of the lithospheric keel (Darbyshire and Eaton 2010).

After providing an overview of the isotropic ambient-noise tomography method, we introduce an anisotropic tomography method that has been previously applied for the inversion of teleseismic surface wave measurements and for array tomography using earthquake signals (Lebedev and van der Hilst 2008; Deschamps et al., 2008; Darbyshire and Lebedev, 2009). Following this, we present the results of anisotropic tomography together with a detailed analysis of parameter selection for the inversion process. Finally, we interpret the inferred anisotropic fabric by comparing our results with stress data, plate-motion directions and regional total-field magnetic anomaly data. Our results indicate that distinct mid-crustal anisotropic fabrics are juxtaposed across a lithospheric suture within the THO.

DATA AND PROCESSING METHODS

The data used for the present study were recorded with a sampling rate of 40 Hz over 21 months, from September 2006 to May 2008. Initial data-processing procedures follow the method of Bensen et al. (2007). First, the continuous vertical-component recordings were cut into individual one-day records and resampled to 1Hz. Next, daily trends, means and instrument-response functions were removed. Earthquake signals and instrument irregularities that could obstruct the signals of interest were suppressed using a one-bit time-normalization procedure. Finally, spectral whitening and bandpass filtering between 0.005 Hz and 0.3 Hz (200 s to 3.33 s period) were applied. Initial data-processing procedures are detailed further by Pawlak et al. (2011).

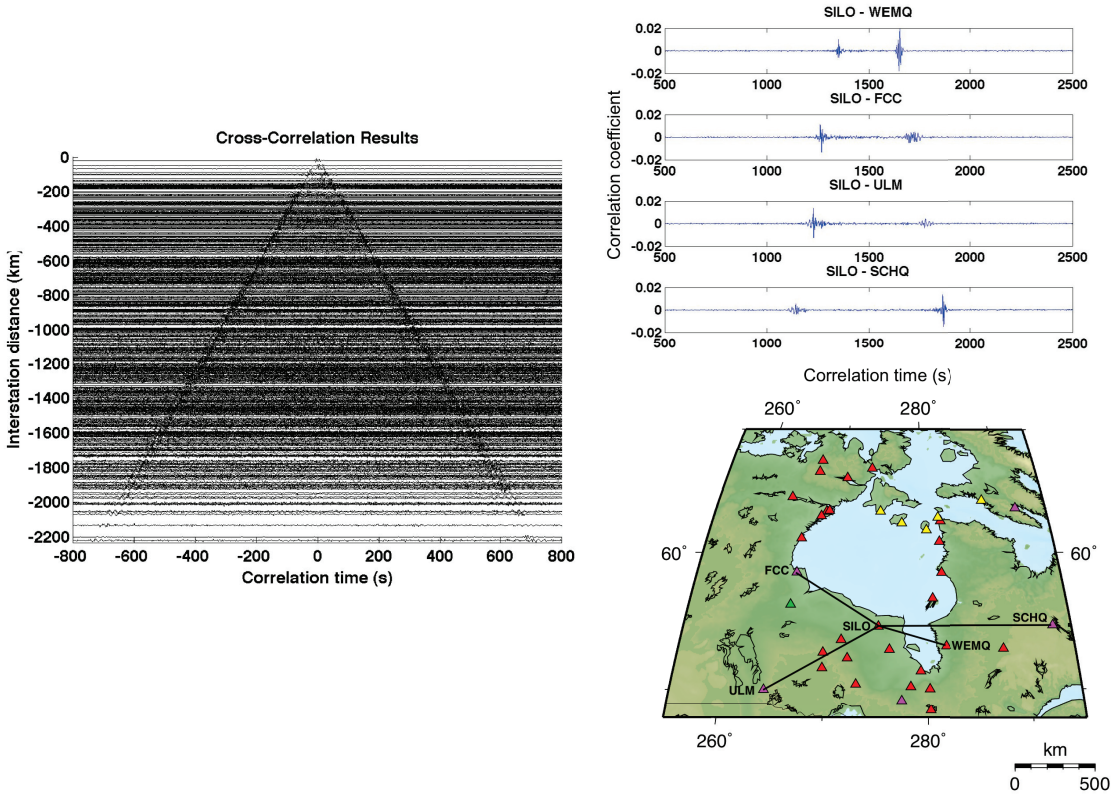

FIG 2. Stacked cross-correlations versus interstation distance for 591 two-station paths (left). Both positive and negative lags are shown. Examples of four cross-correlations (upper right) illustrates asymmetry of correlograms with respect to signal-to-noise ratio (SNR), typical of this dataset. Corresponding paths are shown in the lower right.

After completion of initial processing, correlograms were computed for all possible station pairs using available daily records. For each station pair, stacking of the daily cross-correlated signals yields a band-limited estimate of the inter-station Green's function (Bensen et al. 2007) containing both causal and acausal components (FIG 2). For the vertical-component data in this study, emergent signals are dominated by fundamental-mode Rayleigh waves with periods of ~10-30 s that originate at coastal areas around North America (Pawlak et al., 2011). Based on visual inspection of the stacked correlograms (FIG 2), of 666 available station pairs, 591 were found to be usable.

FIG 2 shows a representative example of a stacked correlogram showing both causal and acausal components of the Green's function. This example exhibits a pronounced asymmetry in which one half of the Green's function is characterized by a conspicuously higher signal-to-noise ratio (SNR) than the other half. This asymmetry originates from an inferred non-uniform distribution of coastal source locations (Pawlak et al., 2011). Since this asymmetry characterizes most of our data, instead of the typical approach (e.g. Bensen et al., 2007) of averaging both sides to obtain a one-sided empirical Green's function (EGF), here we select for further processing the side of the correlogram having higher SNR (Pawlak et al. 2011).

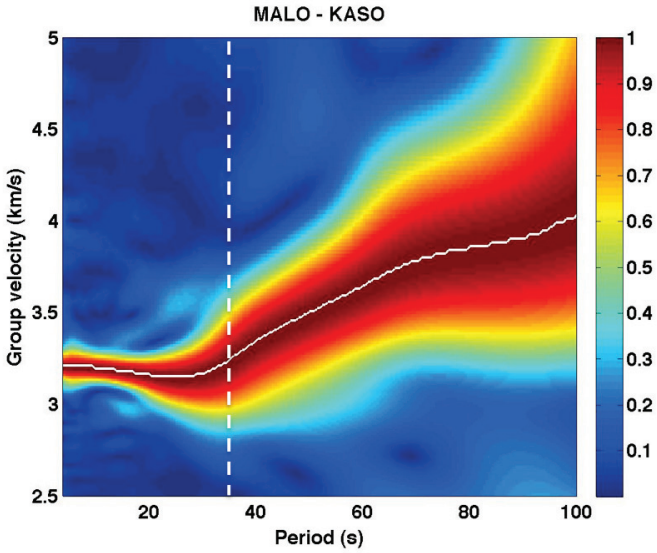

FIG 3. Example time-frequency plot and dispersion analysis. The color scale shows the amplitude envelope, normalized for each period value. The solid white line represents the group-velocity dispersion curve used as input for the inversion procedure. The dashed white line shows an approximate boundary between periods at which group-velocities are sensitive primarily to the crust (left of the line) and primarily to the mantle (right of the line).

The EGFs derived in this fashion were then used for estimating group velocities based on time-frequency analysis (FIG 3). In our implementation of this procedure, the time-frequency plot is constructed for a given central frequency by applying a narrow-band filter to the EGF and then computing the amplitude envelope (Pawlak et al., 2011). Group velocity is obtained as a function of period by tracking the maximum amplitude such that a continuous dispersion curve is obtained. The shape of the dispersion curve is strongly influenced by the thickness of the crust and shows a clear transition from low velocity in the crust to high velocity in the underlying mantle (FIG 3). The group-velocity estimates are used as the basis for tomographic inversions that solve for period-specific models of the fundamental-mode Rayleigh-wave group velocity and azimuthal anisotropy beneath Hudson Bay.

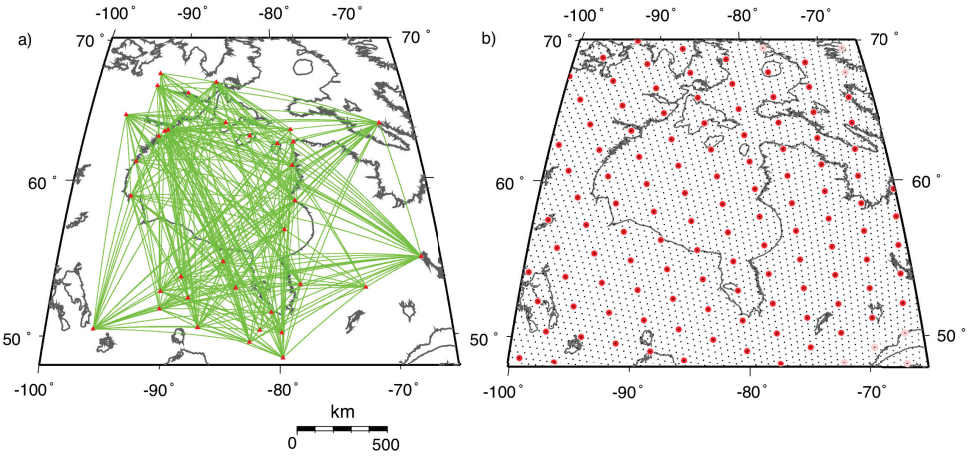

FIG 4. (a) Path density diagram. (b) Map showing model-grid (red circles) and integration-grid (black circles) knots.

INVERSION

We use a tomographic inversion scheme that has already been used—and tested extensively—in analysis of interstation phase-velocity measurements made with teleseismic surface waves (Deschamps et al., 2008; Darbyshire and Lebedev, 2009; Endrun at el. 2011). We remark that, within the usable bandwidth of the data (generally ~10-35 s period for most EGFs in our dataset), the raypath coverage afforded by ambient-noise measurements (FIG 4a) is well suited to anisotropic analysis because it contains nearly the full range of two-station azimuths possible for any given station distribution. The first step is to subtract the mean value of group velocity from all measurements, at each period. For the *i*th station pair, this yields a residual inter-station average group velocity, $\delta U_i(\omega) \pm \Delta U_i(\omega)$, where ΔU_i is the measurement uncertainty (estimated here to be 0.1 km/s). Working at Earth's surface within a spherical co-ordinate system defined by θ, ϕ (FIG 4b), $\delta U_i(\omega)$ can be expressed in terms of the group-velocity model perturbations $\delta U(\omega, \theta, \phi)$ as

$$\int_{\theta}\int_{\phi} K_i(\theta,\phi)\ \delta U(\omega,\theta,\phi)\ d\phi\, d\theta = \delta U_i(\omega) \quad , \tag{1}$$

where ω is angular frequency and K_i defines a sensitivity function for the *i*th station pair. Following Darbyshire and Lebedev (2009), the sensitivity function is defined here by rays along inter-station great-circle paths. To account for the effects of weak Rayleigh-wave anisotropy, the group-velocity perturbations $\delta U(\omega,\theta,\phi)$ are parameterized using 5 unknowns (Smith and Dahlen, 1973):

$$\delta U(\omega) = \delta U_{iso}(\omega) + A_1(\omega)\cos(2\Psi) + A_2\sin(2\Psi) + A_3(\omega)\cos(4\Psi) + A_4(\omega)\sin(4\Psi) \quad , \tag{2}$$

where δU_{iso} is the isotropic group-velocity perturbation and Ψ denotes the wave-propagation azimuth with respect to geographic north. Terms that depend on 2Ψ and 4Ψ in equation (2) account for azimuthal variations of group velocity that exhibit a periodicity of π and $\pi/2$ radians, respectively.

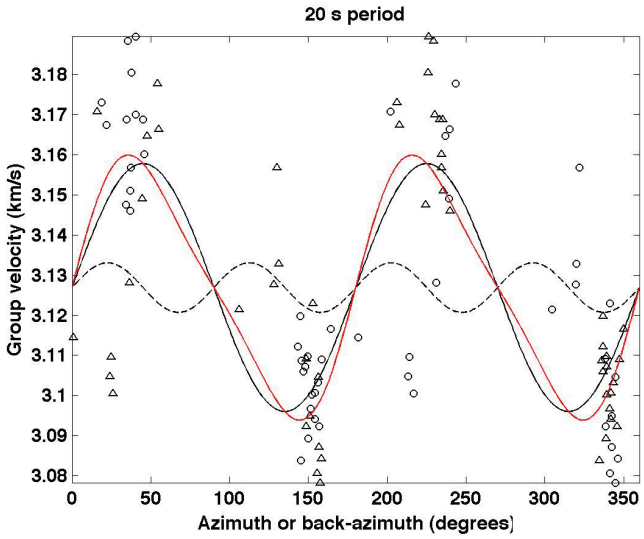

FIG 5. A selection of data taken from an area of dense path coverage at 20 s period. Solid black line represents the L1 norm best fit for 2Ψ variations; the dashed black line is the L1 norm best fit for 4Ψ variation. The red line is theL1 best fit to the data, and the sum of the 2Ψ and 4Ψ variations.

At this stage, we consider a number of simple scenarios to illustrate how 2Ψ and 4Ψ symmetry might relate to fracture systems and/or alignment of intrinsically anisotropic minerals in the continental crust. In evaluating these scenarios, we invoke Neumann's principle (Winterstein 1990) to relate the symmetry properties of the medium to the corresponding symmetry of wave propagation in the medium. For example, a single set of vertical cracks or sheet-like intrusions (dykes) in an otherwise isotropic medium would give rise to an azimuthally anisotropic system that exhibits 2Ψ symmetry for horizontally propagating Rayleigh waves. Crampin (1987) has proposed a more general crustal model, referred to as extensive dilatancy anisotropy, in which pore spaces deform in response to the ambient stress field in a manner that would exhibit the same symmetry behavior as this crack model. Similarly, a 90° periodicity in Rayleigh-wave group velocity implied by the 4Ψ symmetry can be produced by several geologic scenarios. For example, two sets of mutually perpendicular vertical cracks would yield an orthorhombic anisotropic system (Winterstein 1992) with 4Ψ symmetry. A second possibility is a single set of vertical cracks within a transversely isotropic medium, such as crustal rocks with a strong crystallographic preferred orientation as described above.

Given the possible geologic scenarios commonly seen in the crust, our dataset was analyzed to demonstrate whether there are 2Ψ and/or 4Ψ variations. A selection of data taken from an area of dense path coverage at the 20s period is shown in FIG 5. An L1 norm was used to find a best fit to our data points. The solid black line represents the L1 norm best fit for 2Ψ variations and the dashed black line in is the L1 norm best fit for 4Ψ variation. The red line is L1 best fit to the data, and the sum of the 2Ψ and 4Ψ variations. This dataset shows a clear dominance of the 2Ψ signal; therefore from this point forward we will be using the 2Ψ anisotropy results for our interpretations.

The 5 model parameters in equation (2) are computed on a coarse (200 km) triangular model grid (FIG 4b), where the knot-point locations are determined using the method of

Wang and Dahlen (1995). Anisotropy is illustrated using vectors centered at knot points and oriented in the fast-propagation directions, which naturally exhibit the basic π periodicity. The integration used to construct the Equation 1 is performed using a dense (40 km), integration grid of knot points. For every integration knot, a hexagonal region centered on the knot point is considered, whose vertices are made up of the six nearest points. The integration weight is first calculated at each of the integration-grid knot points located within one inter-knot distance from the interstation great-circle path and is proportional to the area of the hexagon around it. The weights K for the model parameters at model grid knots are then computed as integrals over the neighboring integration-grid knots (Lebedev and van der Hilst, 2008).

At each of the 6 selected periods (10, 15, 20, 25, 30, 35 s), a sparse system of linear equations was constructed using Equations 1 and 2 for all available paths. The resulting system was then solved iteratively using LSQR (Paige and Saunders 1982), with smoothing and gradient damping. Model smoothing is based on the difference between the anomaly at a grid knot and the average over anomalies at this and all neighboring knots. Gradient damping is another type of regularization that penalizes the difference between anomalies at each pair of neighboring knot points. The smoothing and damping parameters are assigned independently for δU_{iso} and the 4 anisotropic parameters, and their selection plays a critical role in the inversion.

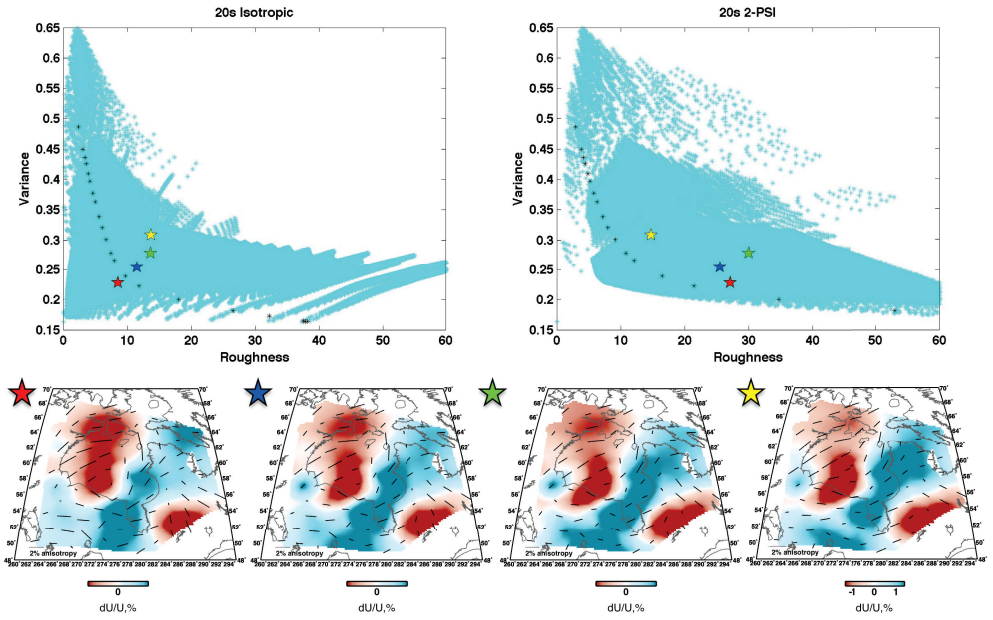

FIG 6. Trade-off curves for isotropic and anisotropic variations for various parameter choices. Data results are shown for parameter choices indicated with the colored stars.

REGULARIZATION PARAMETERS

In this section we test smoothing and damping for both isotropic and anisotropic model parameters. The aim of these tests is to evaluate the significance of parameter coupling ("leakage") in which heterogeneity and anisotropy may trade off with each other in the solution. We begin by examining the effects of smoothing and damping parameters

to explore their influence on the inversion results. These parameters are analyzed by examining the trade-off between model variance and roughness, as shown in FIG 6. The model roughness is the difference between an anomaly at a given grid knot and all nearest-neighbors. FIG 6 shows trade-offs, one for the isotropic velocity and one for the 2Ψ anisotropy, for 20s period. These results are similar for other periods. The black line represents the case in which all parameters are equal and serves solely as a guide for the trend in the curve.

The overall shape of the curve is used as an indication of the behavior of the parameters and provides us with a range of parameter choices. It is desirable to minimize both variance and model roughness simultaneously, since minimizing the variance results in a better fit to the data while minimizing the roughness will reduce artifacts in the result (Schwarzbach et al. 2005). Generally the 'knee', or the bend that minimizes both the variance and the roughness of the trade-off curve, is thought to indicate the best range of parameters and produce the best results for the data (e.g. Moorkamp et al. 2007).

The solutions for a selection of parameters, falling in the general 'knee' zone on both trade-off curves, are shown as stars in FIG 6. The corresponding inversion results are shown below the graphs. Using the Hudson Bay dataset, the parameter values considered fall near the 'knee' zone on both trade-off curves. The isotropic velocity patterns are consistent through all four parameter choices, and are consistent with results found by Pawlak et al. (2011). Anisotropic results generally show the same pattern in all four images. We do see that the red, blue and green star models contain anisotropy directions that form a vortex pattern south of the Bay. This is most likely an artefact due to the parameter choice resulting in higher anisotropic roughness. This artefact does not appear in the yellow star model and thus we choose these parameters as the 'best'. This set of regularization parameters will be used from this point forward.

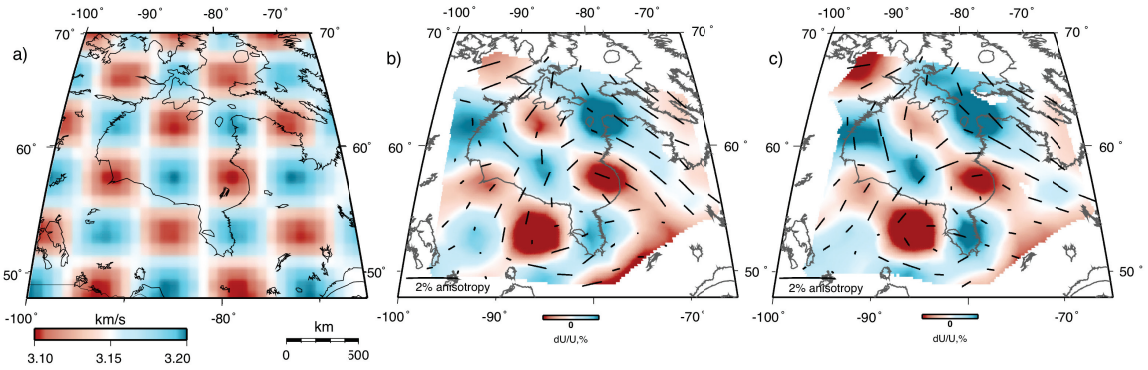

FIG 7. Results for checkerboard resolution tests, a) isotropic checkerboard model, b) isotropic checkerboard reconstruction results for 20s period, c) isotropic checkerboard reconstruction results for 30s periods. Isotropic velocities are well resolved, but with some anisotropy 'leaking' through, for example in the northeast corner.

RESOLUTION TESTING

In order to test the robustness of the isotropic and anisotropic results, two resolution tests were performed. First, a purely isotropic "checkerboard" model was created (FIG 7a), consisting of alternating high-velocity and low-velocity regions. By forward modeling and inversion of the resulting synthetic group velocities, the checkerboard model was reconstructed using the same approach that was used to invert the observations. FIG 7 b and c shows these results for 20 s and 30 s periods, respectively. An important element of this test is 'leakage' of the 2Ψ anisotropy into the model. As mentioned above, the model was purely isotropic, yet the results exhibit spurious anisotropy directions as well. Although the anisotropy is small, it does contain possible artifacts in regions of low path coverage. This can be seen, for example in the northeast corner of both the 20s and 30s maps, where there are northwest-southeast trending anisotropy directions.

To examine the robustness of the models and any possible artificial anisotropy in our results, we performed a second resolution test. This test consists of a model created using isotropic velocities found in our results and anisotropic directions rotated 90 degrees (from a southwest-northeast direction to a northwest-southeast direction). The input patterns were recovered accurately at both 20 s and 30 s periods (FIG 8).

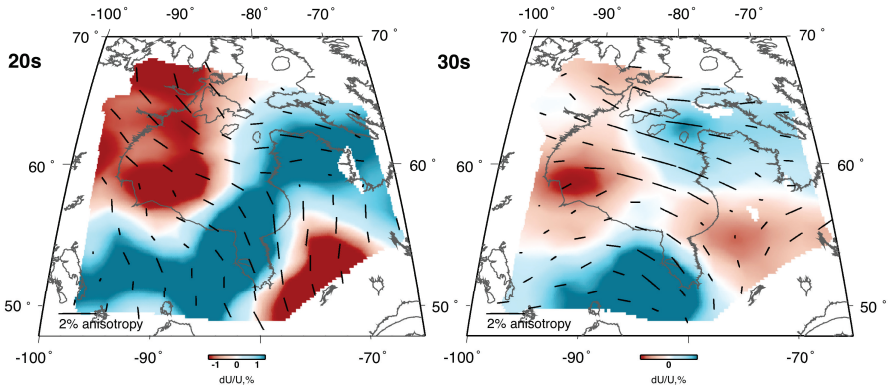

FIG 8. Inversion of anisotropy resolution reconstruction results for 20 s and 30 s periods. The model used for the inversion is the results (shown in figure 8) with the anisotropic fast direction rotated by 90 degrees. This tests for artefacts in the anisotropic patterns due to the unevenness of the path coverage.

RESULTS

Results of the inversion using our preferred parameters are shown in FIG 9. As a rough guideline, the period value in s can be viewed as a proxy for approximate depth of sensitivity in km (Lin et al 2007). Thus, results for 20 s period is representative of mid-crustal velocity structure, whereas results for 30 s is representative of the lower crust. Red denotes lower isotropic velocities and blue denote higher isotropic velocities with respect to the regional average for the given period. Through most of the crust there is a relatively low velocity region within the center of Hudson Bay, as compared with the higher velocities that form a horseshoe shaped region that coincides with the Archean Superior craton (FIG 1b). This regional pattern of isotropic velocity variations is

generally consistent with isotropic tomography results found by Pawlak et al. 2011, which are based on a different tomographic reconstruction method.

Black bars in FIG 9 show the 2Ψ anisotropy fast directions. A predominant southwest-northeast fast direction characterizes the mid-crust (10 s – 20 s period maps), defining an anisotropic fabric that corresponds well with the surface tectonics of the region. Namely, where we observe the horseshoe-shaped Superior craton ("double indentor", Gibb 1983) as defined by relatively fast isotropic velocities, we see the anisotropic fast directions deviate from the dominant northeast-southwest direction to wrap around in accordance with the 'horseshoe' shaped pattern. This feature is most prominent in the 20 s period map. At 25 s period there is a significant transition in anisotropic fast direction to an almost north-south pattern. This pattern persists for longer periods (30 s period), although it is locally rotated (approximately 90 degrees) in the central region in the vicinitiy of the Nastapoka arc (FIG 1b).

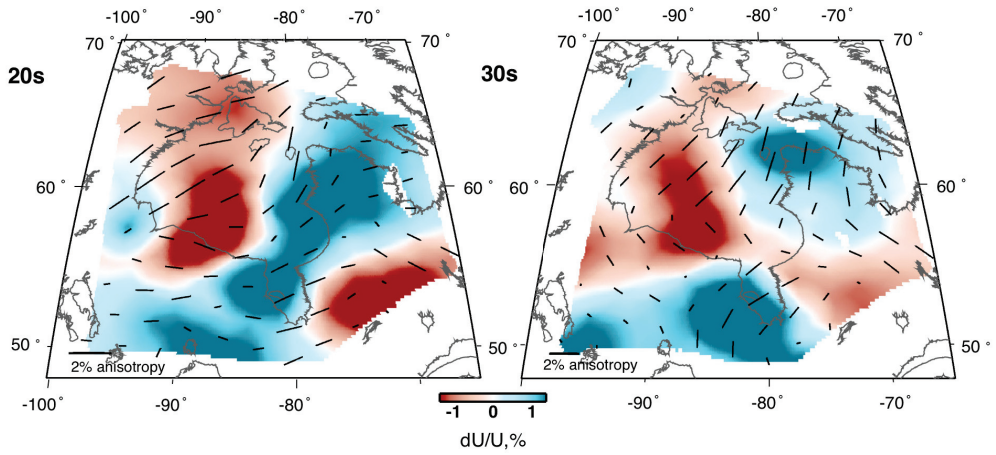

FIG 9. Inversion results for periods 20 s and 30 s. Through most of the crust there is a low relative velocity region within the center of Hudson Bay, as compared with the higher velocities that form a horseshoe shaped region that coincides with the Archean Superior craton (Figure 1b). Anisotropic fast directions are predominantly southwest-northeast in the mid-crust (20 s). There is a significant transition in the lower crust (30 s). Throughout the crust there is a difference in anisotropic fabric on either side of the inferred THO suture zone (FIG1b).

DISSCUSION

Crustal anisotropy studies have previously used shear-wave splitting and/or surface-wave tomography methods. As noted above, various explanations for observed crustal anisotropy have been suggested. Proposed models for anisotropy include alignment of microcracks (Crampin et al. 1984; Kaneshima et al. 1988), preferred mineral alignment (Christensen and Mooney 1995), fossil anisotropy due to the last tectonic event (Wüstefeld et al. 2010; Bastow et al. 2011), plate motion (Bokelmann and Wüstefeld 2009), stress direction (Crampin 1984) and fabrics defined by geologic structures (Lin et al. 2011). In this section, we explore some of these models to help us determine the origin of the anisotropic fabric in our data.

Crustal Stresses

Seismic anisotropy in the crust could be affected by stress direction as a result of preferred opening of microcracks (Crampin 1984). Crustal stress can be approximated from absolute plate motion (APM) directions (Wu 1996) but the direction of plate motion in the study area varies dramatically depending on the reference frame used (e.g. Bastow et al. 2011, FIG 1), making continent-scale conclusions difficult to draw. In any case, the anisotropic fast directions constrained in this study vary over length scales too short to be explained by the APM hypothesis. If the anisotropic fabric is indeed related to crustal stress, a more localized mechanism, such as glacial isostatic adjustment, must be a factor in this area (Steffen et al., 2011).

Stress-field directions have changed in the last 9000 years due to glacial rebound stress following the last ice age (Wu 1996). However, the principal horizontal stresses at 9 ka and at the present projected from rebound stress including tectonic and overburden stresses, are very similar in the Hudson Bay region (Wu 1997). Within the Bay these directions are NE-SW, similar to the dominant direction found in both our mid-crustal (20s period) and lower crustal (30s period) maps.

More recent studies analyzed moment tensor inversion from local earthquakes to infer the inherent stress field (Steffen et al. 2011). Using data from five earthquakes in northern Hudson Bay Steffan et al., (2011) show NNE-SSW directed maximum horizontal stress direction. Although this study is slightly north of our study area, it is generally consistent with our principal anisotropic fast directions.

The crustal stress directions support the anisotropic fast directions seen in our data, but have longer wavelength. This alignment with crustal stresses is apparent mainly in the upper to mid crust. This could mean that the aligned microcracks or single direction foliation is dominant in the background but a smaller wavelength feature appears near the centre of the bay at the suture zone. Perhaps the deformation that occurred at the time of collision is creating these shorter wavelength features.

Magnetic Data

Magnetic data have been used in recent years in relation to seismic anisotropy (Bokelmann and Wüstefeld 2009; Wüstefeld et al. 2010). Due to the limiting temperature for ferromagnetic behavior and the depth decay ($1/r^3$), magnetic data is well suited for studies of the uppermost lithospheric fabrics (Bokelmann and Wüstefeld 2009). Previous studies found a relation between seismic anisotropy in the mantle from shear wave splitting results compared with crustal magnetics. This relation is consistent with vertically coherent deformation, in which the crust and mantle deform as a unit (Silver and Chan 1988). Since ambient-noise studies are confined to the crust and uppermost mantle, comparing crustal magnetic features is appropriate.

Magnetic data are available from the Geological Survey of Canada (FIG 10; GSC 2010). This assemblage of aeromagnetic and marine data is presented on a 400 m grid. Comparing the magnetic data and the 20 s period anisotropic results, there is a very similar pattern in the center of the Bay, showing a possible effect from the tectonic boundaries. This indicates that the crust at these depths is likely to have retained an anisotropic structure that dates back to the time of crustal formation in the Archean. The

30 s period anisotropy, however, appears to have little correlation to the magnetic data, suggesting there is little-to-no vertically coherent deformation between the crust and upper mantle or within the crust as was suggested by Bokelmann and Wustefeld (2009), or perhaps a disconnect in the lower crust only. This would be similar to the strong depth dependence of deformation patterns and anisotropy seen in some of the regions deforming today (e.g., Endrun et al., 2011).

While the anisotropic signature of the brittle shallow crust may have retained an anisotropic signature since formation in the Archean, the ductile lower crust/upper mantle anisotropic observations appear more sensitive to major mountain building events such as the THO, as is observed in the SKS studies of mantle anisotropy. One big similarity between all the datasets is that there does appear to be a significant change in anisotropic direction on either side of the suture zone (shown with the red arrows on the magnetic data, FIG 10). This change suggests a possible frozen anisotropic fabric before the collision between the Superior Craton and the Churchill Province. This also suggests little to no deformation since the collision.

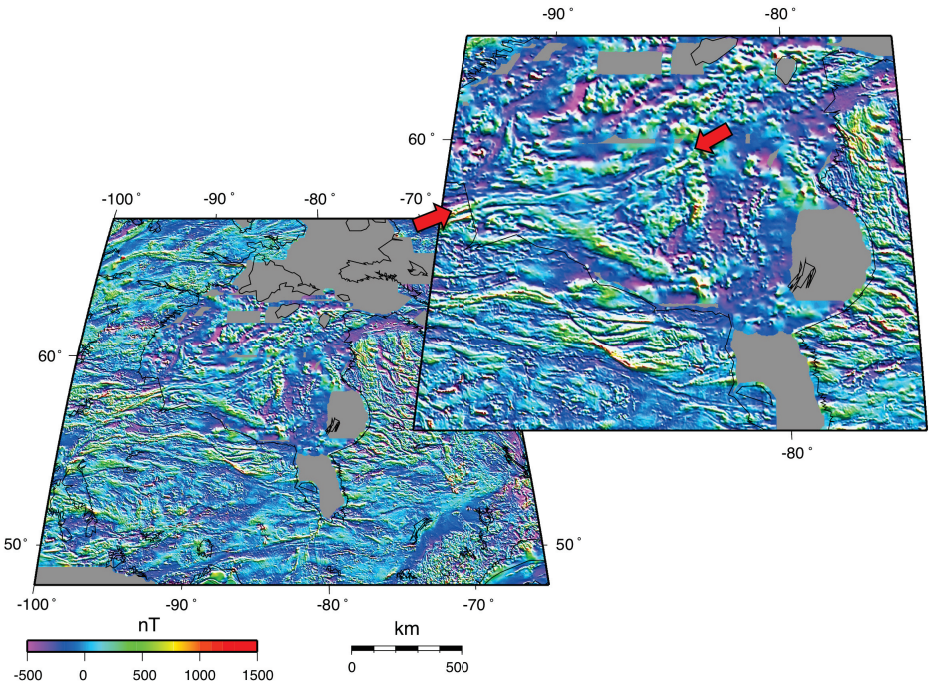

FIG 10. Shaded relied image of regional total-field magnetic anomaly data (left). An enlargement of Hudson Bay highlights the magnetic response along the suture zone, indicated by the red arrows.

CONCLUSIONS

This study is one of the first to use ambient-noise data has been used to investigate crustal anisotropy. The inversion method uses smoothing and damping parameters to regularize the solution; however, due to the significantly increased number of model parameter relative to the isotropic case, considerable attention has been given to investigating whether “leakage” occurs between the isotropic and anisotropic parameters in the inversion. Isotropic velocity patterns found in this study are consistent with results

found by Pawlak et al. (2011). Based on analysis of the raw data, 4Ψ anisotropy appears to be negligible for the periods of main interest, allowing us to focus on 2Ψ results. This is consistent with certain forms of anisotropy, such as azimuthal anisotropy in hexagonal symmetry systems caused by a single set of aligned cracks, or metamorphic fabrics associated with LPO of certain minerals.

The 20 s result generally follows the regional stress field found in the area from rebound stress, although there are smaller wavelength features in the anisotropy data than in the known crustal stress distributions. The smaller wavelength features align well with magnetic fabric and show a change across an inferred suture zone that runs through the centre of the Bay. This may suggest that the background of this region is dominated by aligned cracks or single direction foliation in both the Superior and Churchill domains but that the deformation due to collision at the suture zone is dominating the centre of the Bay.

In the 30 s result, representative of the lower crust, we observe a significant change in anisotropic pattern. Although some studies have shown vertically coherent deformation between the mid-crust and upper mantle; our observations suggest independent deformation in the lower crust, possibly due to channel flow, after the original deformation. This idea would support a 'jelly sandwich' rheologic model in the Hudson Bay region. We also see a significant difference in anisotropy on either side of the suture at all periods, suggesting that the deformation recorded by anisotropy within the crust of the Superior Craton is likely to be pre-collisional.

ACKNOWLEDGEMENTS

We are grateful to Dr. Honn Kao, from the Pacific Geoscience Center in Sydney, B.C., for providing us with initial data and assistance with data processing. We thank other members of the HuBLE working group for stimulating discussions and the CREWES project and CREWES sponsors at the University of Calgary for their support. Thank you to C-NGO and the First Nation communities around Hudson Bay for allowing seismometer deployments. GMT (Wessel and Smith, 1995) and dispersion code written by R. Herrmann was used in the preparation of some figures. Natural Environment Research Council (NERC) stations, for this project, are supported by grant No. NE/F007337/1. This study was supported by NSERC through a Discovery Grant to DWE. IB was funded by the Leverhulme Trust.

REFERENCES

Bastow, I.D., D., Thompson, J., Wookey, J.M., Kendall, G., Helffrich, D., Snyder, D.W., Eaton and F.A. Darbyshire, 2011, Precambrian plate tectonics: Seismic evidence from northern Hudson Bay, Canada: Geology, 39, 91-94, doi: 10.1130/G31396.1.

Bensen, G.D., Ritzwoller, M.H., Barmin, M.P., Levshin, A.L., Lin. F., Moschetti, M.P., Shapiro, N.M. and Yang, Y., 2007. Processing seismic ambient noise data to obtain reliable broad-band surface wave dispersion measurements: Geophys. J. Int, 169, 1351-1375.

Bokelmann, G.H.R. and A. Wüstefeld, 2009, Comparing crustal and mantle fabric from the North American craton using magnetics and seismic anisotropy: Earth Planet. Sci. Lett., 277 (3-4), 355-364.

Christensen, N.I. and W.D. Mooney, 1995, Seismic velocity structure and composition of the continental crust: A global view, J. Geophys. Res., 100, 9761-9788.

Crampin, S., 1984. An introduction to wave propagation in anisotropic media; Geophys. J. R. astr. Soc., 76, 17-28.

Crampin, S., E.M., Chesnokov and R.G., Hipkin, 1984. Seismic anisotropy – the state of the art: II; Geophys. J. R. astr. Soc., 76, 1-16.

Crampin, S., 1987. Geological and industrial implications of extensive-dilatancy anisotropy; Nature, 328, 491 – 496.

Crampin, S., 1994. The fracture criticality of crustal rocks; Geophys. J. Int., 118, 428-438.

Curtis, A., P. Gerstoft, H. Sato, R. Snieder, and K. Wapenaar, 2006, Seismic interferometry – turning noise into signal: The Leading Edge, 1082-1092.

Darbyshire, F.A. and S. Lebedev, 2009. Rayleigh wave phase-velocity heterogeneity and multilayered azimuthal anisotropy of the Superior Craton, Ontario; Geophys. J. Int., 176, 215-234.

Darbyshire, F. and D.W., Eaton, 2010, The lithospheric root beneath Hudson Bay, Canada from Rayleigh-wave dispersion: No clear seismological distinction between Archean and Proterozoic mantle, Lithos, doi:10.1016/j.lithos.2010.04.010.

Deschamps, F., S. Lebedev, T. Meier, J. Trampert, 2008, Azimuthal anisotropy of Rayleigh-wave phase velocities in the east-central United States, Geophys. J. Int., 173, 827-843.

Eaton, D.W. and F.A. Darbyshire, 2010, Lithospheric architecture and tectonic evolution of the Hudson Bay region: Tectonophysics, 480, 1-22.

Endrun, B., S., Lebedev, T., Meier, C., Tirel and W., Friederich, 2011, Complex layered deformation within the Aegean crust and mantle revealed by seismic anisotropy: Nature Geoscience, 4, 203-207, doi:10.1038/ngeo1065.

Gibb, R.A., 1983. Model for suturing of Superior and Churchill plates: an example of double-indentation tectonics. Geology 11, 413–417.

GSC, 2010, Canadian Aeromagnetic Data Base, Airborne Geophysics Section, GSC - Central Canada Division, Geological Survey of Canada, Earth Sciences Sector, Natural Resources Canada Contact: http://gdcinfo.agg.nrcan.gc.ca/contact_e.html#DataCentre

Kaneshima, S., M., Ando and S., Kimura, 1988. Evidence from shear-wave splitting for restriction of seismic anisotropy to the upper crust: Nature, 335, 627-629.

Lebedev, S. and R.D. van der Hilst, 2008, Global upper-mantle tomography with the automated multimode inversion of surface and S wave forms: Geophys. J. Int., 173, 505-518.

Lin, F.C., M.H. Ritzwoller, J. Townend , M. Savage, and S. Bannister, 2007, Ambient noise Rayleigh wave tomography of New Zealand: Geophys. J. Int.,170, 649–666, doi:10.1111/j.1365-246X.2007.03414.x.

Lin, F.C., M.H. Ritzwoller, Y. Yang, M.P. Moschetti and M.J. Fouch, 2010, Complex and variable crustal and uppermost mantle seismic anisotropy in the western United States: Nature Geosci, 4, doi: 10.1038/NGE01036.

Moorkamp, M., A.G., Jones and D.W., Eaton, 2007, Joint inversion of teleseismic receiver functions and magnetotelluric data using a genetic algorithm: Are seismic velocities and electrical conductivities compatible?: Geophys. Res. Lett., 34, doi:10.1029/2007GL030519.

Moschetti, M.P., M.H. Ritzwoller, and N.M. Shapiro, 2007, Surface wave tomography of the western United States from ambient seismic noise: Rayleigh wave group velocity maps: Geochem., Geophys., Geosys., 8.

Paige, C.C. and M.A. Saunders, 1982, LSQR: an algorithm for sparse linear equations and sparse least squares: Assoc. Comput. Mach. Trans. Math. Software, 8, 43-71.

Paulssen, H., 2004. Crustal anitsotropy in southern California from local earthquake data; Geophys. Res. Lett., 31, doi:10.1029/2003GL018654.

Pawlak, A.P., D.W. Eaton, I.D. Bastow, J.M. Kendall, G. Helffrich, J. Wookey and D. Snyder, 2011, Crustal structure beneath Hudson Bay from ambient-noise tomography: Implications for basin formation: Geophys. J. Int., 184, 65-82, doi:10.1111/j.1365-246X.2010.04828.x

Shapiro, N.M., M. Campillo, L. Stehly, and M.H. Ritzwoller, 2005, High resolution surface wave tomography from ambient seismic noise: Science, 307, 1615-1618.

Silver, P.G. and W.W. Chan, 1988, Implications for crustal structure and evolution from seismic anisotropy. Nature, 335, 34-39.

Smith, M.L. and F.A. Dahlen, 1973, The azimuthal dependence of Love and Rayleigh wave propagation in a slightly anisotropic medium: J. Geophys, Res., 78, 3321-3333.

Smith, D.B., M.H., Ritzwoller and N.M., Shapiro, 2004. Stratification of anisotropy in the Pacific upper mantle

Schwarzbach, C., R.U., Börner and K., Spitzer, 2005, Two-dimensional inversion of direct current resistivity data using a parallel, multi-objective genetic algorithm: Geophys. J. Int., 162, 685-695, doi:10.1111/j.1365-246X.2005.02702.x .

Thompson, D.A., I.D. Bastow, G. Helffrich, J.M. Kendall, J. Wookey, D.Snyder and D.W. Eaton, 2010, Precambrian crustal evolution of the Canadian Shield: Constraints from receiver function analysis, Earth Planet. Sci. Letts, 297, 655-666, doi:10.1016/j.epsl.2010.07.021.

Wang , Z., and F.A., Dahlen, 1995, Spherical-spline parameterization of 3-dimensional earth models, Geophys. Res. Lett., 22, 3099-3102.

Wessel, P and W.H.F., Smith, 1995, New Version of the Generic Mapping Tools Released, EOS Trans. AGU, 76, 329.

Winterstein, D.F., 1990. Velocity anisotropy terminology for geophysicists; Geophysics, 55, 1070-1088.

Winterstein, D., 1992. How shear-wave properties relate to rock fractures: Simple cases: The Leading Edge, 11, 9, 21-28.

Wu, P., 1996, Changes in orientation of near-surface stress field as constraints to mantle viscosity and horizontal stress differences in Eastern Canada. Geophys. Res. Lett., 23, 2263-2266.

Wu, P., 1997, Effect of viscosity structure on fault potential and stress orientations in eastern Canada. Geophys. J. Int., 130, 365-382.

Wüstefeld, A., G. Bokelmann and G. Barruol, 2010, Evidence for ancient lithospheric deformation in the Eat European Craton based on mantle seismic anisotropy and crustal magnetics. Tectonophysics, 481, 16-28.

Yang, Y., M.H. Ritzwoller, A.L. Levshin, and N.M. Shapiro, 2007, Ambient noise Rayleigh wave tomography across Europe. Geophys. J. Int., 168, 259-274, doi:10.1111/j.1365-246X.2006.03203.x.

Yao, H., R.D. van der Hilst, and M.V. de Hoop, 2006, Surface-wave tomography in SE Tibet from ambient seismic noise and two-station analysis: I.- Phase velocity maps. Geophys. J. Int., 166, 732-744.